



# Quasi-BICs Enabled Proximity Sensing Based on Metal Complementary H-Shaped Arrays at Terahertz Frequencies

Lele Wang, Jun Cao, Xiaowen Li, Yanliang Zhao, Hui Shi, Liping Fu, Dejun Liu , and Feng Liu 

**Abstract**—All metal sensing based on complementary H-shaped arrays (HSAs) is numerically and experimentally investigated at terahertz frequencies. The symmetry-protected bound states in the continuum (BICs) are activated by adjusting one arm's length of the H-shaped, enabling high- $Q$  quasi-BICs. The  $Q$ -factor of quasi-BICs is modulated in terms of structural parameters and metal conductivity. With optimal structural parameters of copper HSAs, the proximity sensing performances are studied as a function of the film thickness and the refractive index. High sensitivity of 151 GHz/RIU and FOM of 18.7 are obtained, respectively, which are high compared with the previous metamaterials with planar substrates. In addition, the HSAs are even sensitive to the ultrathin graphene film. These findings indicate that such HSAs-based sensor has great potential for practical applications in chemical and biomolecular fields.

**Index Terms**—All-metal metasurfaces, bound states in the continuum, terahertz sensing.

## I. INTRODUCTION

**B**OUND states in the continuum (BICs) are localized mode that exists in continuous-wave radiation in free space. BICs are first proposed in quantum by *von Neumann and Wigner mechanics* in 1929 and later are found to occur in various fields such as acoustics, microwaves, and nano-photonics [1], [2], [3], [4], [5], [6], [7], [8], [9], [10]. The BICs are characterized by its ultra-narrow bandwidth and ultra-high quality ( $Q$ ) factor. The  $Q$

value of BICs in an ideal state tends to be infinite, which can increase the time order of magnitude of the interaction between light and matter. When both the  $Q$ -factor and the resonant width become limited, BICs turn into quasi-BICs or the so-called super cavity modes [11], which appear as a Fano line with an ultra-high  $Q$  value [12], [13], [14], [15], [16], [17], [18]. The quasi-BICs offers great potential for application in the fields of ultra-sensitive sensors [18] and ultra-narrowband filters [16], [19], [20], [21], [22], [23].

Quasi-BICs with high  $Q$ -factors have giant potential in terahertz (0.1–10 THz) applications such as electromagnetic wave manipulation and sensing [24], [25]. THz waves have considerably low photon energy (4.1 meV at 1 THz) and cannot lead to photoionization in biological tissues as can X-rays, proven to be well suited for diagnostics and imaging of biological tissues [24]. THz waves are also suitable to drive and probe intermolecular forces, opposite to the feasibility of the IR radiation to perturb intra-molecular attractions, therefore enabling spectroscopic fingerprinting for molecules. Thus, THz technology is promising to be used in an increasingly wide variety of applications including sensing, communications, biomedical sciences, homeland security, and quality control, in addition to medical diagnostics [25]. Recently, many components with high  $Q$ -factors have been proposed for THz sensing. S. Han et al. designed a purely Si THz resonator, which achieves high  $Q$ -factor super cavity resonant modes near the BICs by varying the length of the Si resonator [26]. But for dielectric or semiconductor resonators, the modal fields are confined in the resonator, resulting in low light-matter interaction volumes. In 2019, Y. K. Srivastava et al. realized 7-nm analytes THz sensing by quasi-BICs found in metasurface [27]. Owing to the surface plasmon polaritons (SPPs) trapped at the metal edges, the interaction between SPP fields and the analyte is enhanced. In 2020, X. Chen et al. reported a new terahertz nanofilm sensor with both toroidal dipoles and BICs, achieving a sensitivity of amplitude difference of 0.32/RIU [28]. Previous studies demonstrated that material absorption is crucial to sensing performance, which led to the sensor exploration in favor of ultrathin substrates [29], [30], [31]. Ultrathin substrates led to an order of magnitude improvement in the sensitivity of the planar THz metamaterial sensors and need high-resolution fabrication processing. Another way to eliminate the additional material absorption from substrates is using all-metal structures. The fabrication of all-metal structures using laser systems is

Manuscript received 23 June 2022; revised 5 September 2022; accepted 13 September 2022. Date of publication 19 September 2022; date of current version 27 September 2022. This work was supported in part by Shanghai Pujiang Program under Grant 20PJ1412200, in part by the Program of Shanghai Academic Research Leader under Grant 22XD1422100, in part by the National Nature Science Foundation of China under Grants 62205211, 12073018, 12141303, U1931205, and 11933002, in part by the Science and Technology Commission of Shanghai Municipality under Grants YDZX20203100002498, 19590746000, 20070502400, and 20142200600, in part by the Dawn Program under Grant 19SG41, and in part by the Innovation Program of Shanghai Municipal Education Commission under Grant 2019-01-07-00-02-E00032. (Corresponding authors: Liping Fu; Dejun Liu; Feng Liu.)

Lele Wang, Jun Cao, Xiaowen Li, Yanliang Zhao, Hui Shi, and Liping Fu are with the Department of Physics, Shanghai Normal University, Shanghai 200234, China (e-mail: 978741691@qq.com; huskie@idealfuture.org.cn; liwen\_phy@163.com; yanliang.zhao@foxmail.com; huishi@shnu.edu.cn; fuliping@shnu.edu.cn).

Dejun Liu and Feng Liu are with the Department of Physics, Shanghai Normal University, Shanghai 200234, China, and also with the Shanghai Key Laboratory for Submillimeter Astrophysics, Shanghai Normal University, Shanghai 200234, China (e-mail: dejunliu1990@shnu.edu.cn; fliu@shnu.edu.cn).

Digital Object Identifier 10.1109/JPHOT.2022.3207172

convenient and cheap, which efficiently reduces the complex fabrication process. For example, R. Yahiaoui et al. proposed a sensor based on metal hole arrays. Results show that the frequency shift reaches a relatively high value of about 125 GHz [32]. In addition, compared to these metamaterials or metasurfaces for disposable sensing, all-metallic structure-based sensors are reusable because it is easy to clean with acetone and alcohol after being used for material sensing [33]–[34]. In 2020, Liu et al. proposed a metasurface based on 3D metal woven meshes, realizing a high  $Q$ -factor of 47 [35]. Result reveals that metal woven meshes improve the surface field of metal hole array for THz sensing. By using more sharp resonances, the sensitivity of all-metal sensors can be improved [36], [37], [38]. Thus, introducing the quasi-BICs with high  $Q$ -factors is highly desirable for all-metal metasurfaces in THz sensing.

Here, based on the advantages of H-shaped structures [39], we have investigated the symmetry-protected BICs in a terahertz all-metal metasurface. The quasi-BICs are realized when the symmetry is broken. Our study shows that the  $Q$ -factor can be modulated by the asymmetry parameters and the metal conductivity. Experimental results show that the proposed HSAs achieve a high  $Q$ -factor of 75. The sensing performance of HSAs is further investigated by varying the dielectric film thickness, the air gap, and the refractive index. High sensitivity of 151 GHz/RIU and FOM of 18.7 are obtained, respectively, which is higher than that of previous metamaterials with planar substrates. In addition, the induced quasi-BIC in HSAs is sensitive to the ultra-thin graphene film. These findings indicate that the sensor has great potential for practical applications in chemical and biomolecular areas.

## II. MATERIALS AND METHODS

### A. Structural Configurations and Measured Results

The proposed HSAs are etched from a copper plate ( $50\ \mu\text{m}$ ) by a femtosecond laser system [40]. Compared to dielectric-based metamaterials or metasurfaces, the HSAs has the advantages of stable performance, durability, and low cost. The 3D schematic of HSAs with a layer of analyte is plotted in Fig. 1. Different from the H-shaped structure in reference [39] with an arm length that equals one period, the length of the arm in our proposed H-shaped structure is short than one period. As shown in Fig. 1(a), the electric fields of the input transverse magnetic wave (TM) and transverse electric wave (TE) parallel to the X-axis and Y-axis are set, respectively. The structural parameter definitions and the photo of the samples are also depicted in Fig. 1(a). The structural parameters are expressed as follows:  $W = 60\ \mu\text{m}$ ,  $L = 200\ \mu\text{m}$ ,  $\Lambda = 260\ \mu\text{m}$ . In the finite-difference-time-domain (FDTD) method, the boundaries in the X- and Y- directions are set as the periodic boundary, and the perfectly matched layers (PML) with minimum PML set to 64 along the Z-direction are defined. The material of the HSAs is set to copper with a conductivity of  $5.96 \times 10^7\ \text{S/m}$ . The mesh size in X-, Y-, and Z-directions is set as 0.01 mm, 0.01 mm, and 0.005 mm, respectively. As demonstrated in previous reports [36], [37], [38], for the aperture structures, the sharp resonance can be induced when an oblique wave is applied. But this resonance

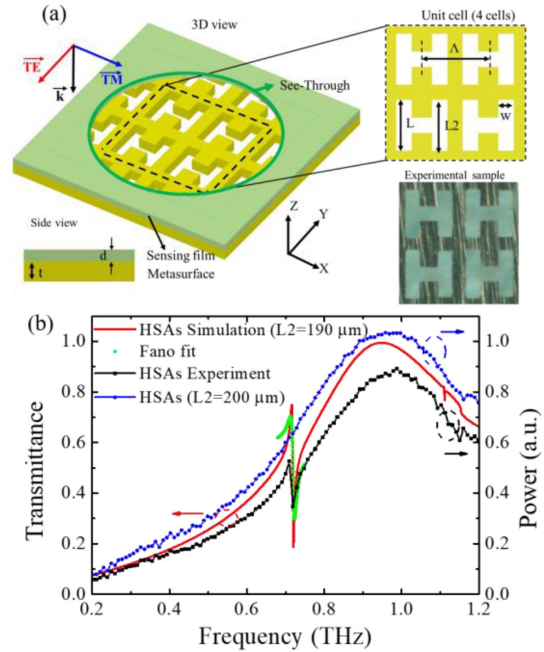


Fig. 1. (a) 3D schematic of the sensing model based on the H-shaped arrays (HSAs), where a dielectric film is covered on the HSAs. The unit cell of HSAs, the side view of the sensing model, and the photo of experimental samples are depicted, where the  $L_2$  is  $190\ \mu\text{m}$ . (b) Experimental and simulated transmittance spectra of TE modes for HSAs with  $L_2 = 190\ \mu\text{m}$  and  $200\ \mu\text{m}$ .

is limited in practical sensing because it needs precise angle control. Thus, another way to obtain a sharp resonance is highly desirable. The H-shape structure is a symmetric structure when both  $L$  and  $L_2$  are set as  $200\ \mu\text{m}$ . The corresponding spectrum of TE modes is the same as that of TM modes. The symmetry of HSAs can be broken by increasing or reducing the length of one arm in the H-shape structure. In other words, we can change the length of  $L_2$  to break the symmetry of HSAs. Fig. 1(b) shows the transmittance spectrum of HSAs for TE modes, where the slit length  $L_2$  reduces to  $190\ \mu\text{m}$ . In contrast to the symmetric HSAs ( $L_2 = 200\ \mu\text{m}$ ), a significant resonant dip with an asymmetric profile can be observed at  $0.72\ \text{THz}$ , where the simulated dip agrees well with that experimental dip. The simulated  $Q$ -factor of such dip reaches 180, which is higher than the measured one of 75 because the simulated resolution reaches  $1\ \text{GHz}$  [41]. But the measured  $Q$ -factor is limited by the sweep resolution ( $9.6\ \text{GHz}$ ) of THz-TDS, which can be improved by using a higher resolution one [42]–[43]. This obtained  $Q$ -factor is much higher than that of previous studies [44]–[45]. For instance, the proposed metasurface in [44] realizes a measured  $Q$ -factor of 20. Increasing the length of  $L_2$  can also break the structural symmetry of HSAs. These results suggest that a slight change in HSAs can achieve high  $Q$ -factor resonances. Such sharp resonance with low transmittance can be excited by TE modes rather than TM modes, whose profile resembles that of Fano resonances [46]. We have used a Fano line shape to fit such resonance, which is given by

$$T = \left| a_1 + ja_2 + \frac{b}{\omega - \omega_0 + j\gamma} \right|^2 \quad (1)$$

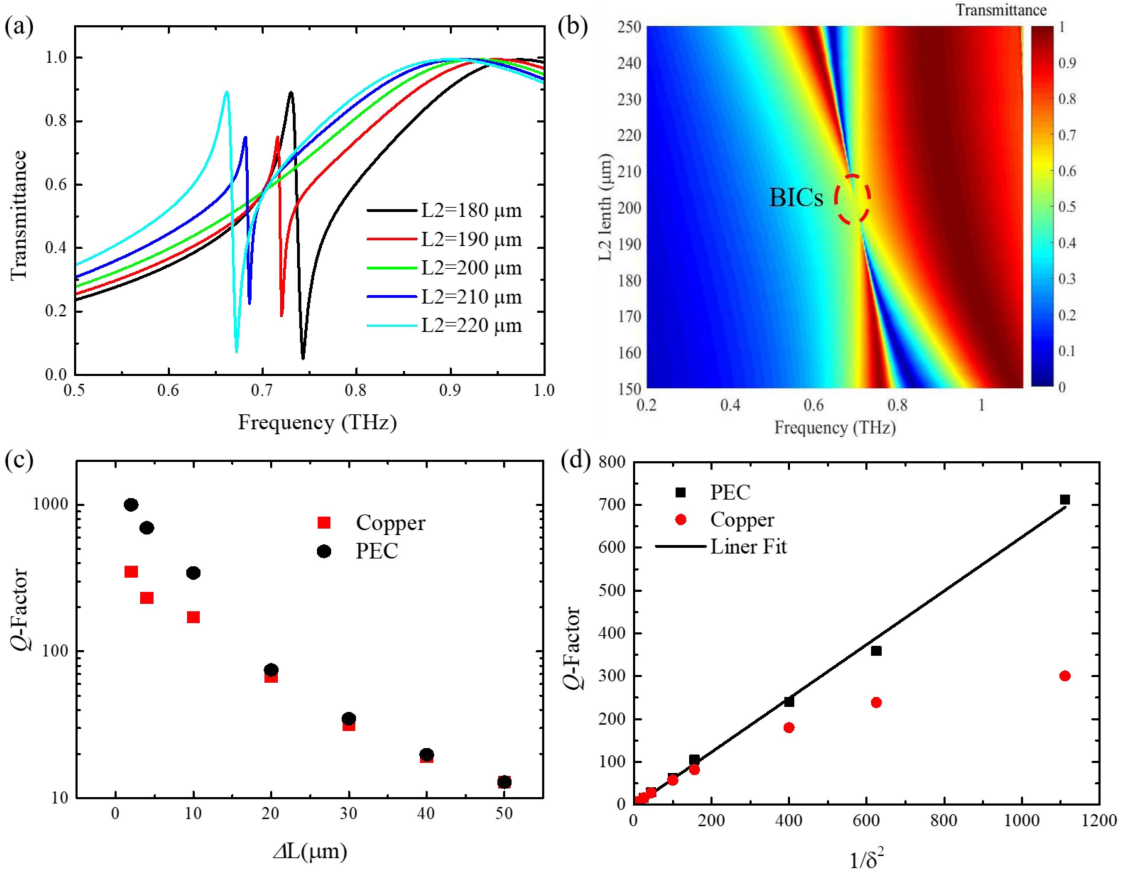


Fig. 2. (a) Transmittance spectra of HSAs with various  $L_2$ . (b) Simulated transmittance spectra map of copper HSAs with varying  $L_2$ . (c) Dependence of  $Q$ -factor on  $\Delta L$ . (d) Linear relationship between  $Q$ -factor and  $1/\delta^2$ . The black line is a linear fitting line.

where  $a_1$ ,  $a_2$ , and  $b$  are constant real numbers;  $\omega_0$  is the central resonant frequency; and  $\gamma$  is the overall damping rate of the resonance [47]. The simulated results are well fitted by this equation. The HSAs can be used as sensors in THz sensing due to their high  $Q$ -factors. In contrast to the sensors based on metasurfaces with high cost, the free-standing HSA is very cheap and thus suitable for low-cost sensing.

### B. Sharp Quasi-BICs in Terms of the Structural Parameters and Material Features

We have investigated the spectral response of HSAs by varying the length of  $L_2$  with a step of  $10 \mu\text{m}$ , which is shown in Fig. 2(a). From  $180 \mu\text{m}$  to  $220 \mu\text{m}$ , as  $L_2$  gradually increases, the resonant dip shifts to lower frequencies. Specially, when the  $L_2$  ups to  $200 \mu\text{m}$ , the resonant dip vanishes. This disappeared resonance occurs in the symmetric HSAs, which is due to symmetry-protected BICs with infinite  $Q$ -factors [48]. Once the structural symmetry is broken, the symmetry-protected BICs changes to the quasi-BICs with finite  $Q$ -factors, representing a bound state couple to the extended waves and leaking out. With the decreasing of  $L_2$ , the resonant dip is induced again and shifts to lower frequencies. Hence, the appearance of BICs is tightly correlated with the value of  $L_2$ . The phenomenon of BICs changes to quasi-BICs can be seen clearly in the transmittance spectral map of HSAs with a variation of  $L_2$ , which is shown in

Fig. 2(b). From  $250 \mu\text{m}$  to  $200 \mu\text{m}$ , the bandwidth of quasi-BICs becomes narrower as  $L_2$  decreases. The resonance becomes sharper and finally disappears when  $L_2$  is equal to  $200 \mu\text{m}$ . That vanished resonance corresponds to a BIC state [48]. As  $L_2$  further decreases, quasi-BICs appear again and its resonant width becomes wider. When  $L_2$  deviates from  $200 \mu\text{m}$ , in other words, the symmetry of HSAs is broken, quasi-BICs are then occurred and exhibited an asymmetric profile of Fano resonances with finite  $Q$ -factors. Therefore, the quasi-BICs can be manipulated by changing  $L_2$ . We have summarized the relation of the  $Q$ -factor with  $\Delta L$  in Fig. 2(c), where  $\Delta L = L_2 - L$ . Here, the HSAs made of the perfect electrical conductor (PEC) and copper are demonstrated. As the gradual increases  $\Delta L$ , the  $Q$ -factor of both PEC and copper HSAs decreases exponentially, which is in the quasi-BIC stage. When  $\Delta L$  is close to  $0 \mu\text{m}$ , the  $Q$ -factor tends to infinity, which means that the ideal BIC is achieved. Obviously, copper-HSAs show lower  $Q$ -factors than that of PEC-HSAs when  $\Delta L$  is smaller than  $20 \mu\text{m}$ . It means that the  $Q$ -factors of quasi-BICs are giant affected by the material loss in this region. However, when  $\Delta L$  is larger than  $20 \mu\text{m}$ , PEC-HSAs show the same level of  $Q$ -factors as copper ones although PEC is without Ohmic loss. Fig. 2(d) shows the relationship between  $Q$ -factor and  $1/\delta^2$ , where the asymmetry parameter  $\delta$  is defined as  $\delta = \Delta L/L$ . For PEC-HSAs, the  $Q$ -factor can be fitted by clearly inverse quadratic law ( $Q \propto 1/\delta^2$ ) very well, which agrees well with previous studies [16]. The quadratic scalability

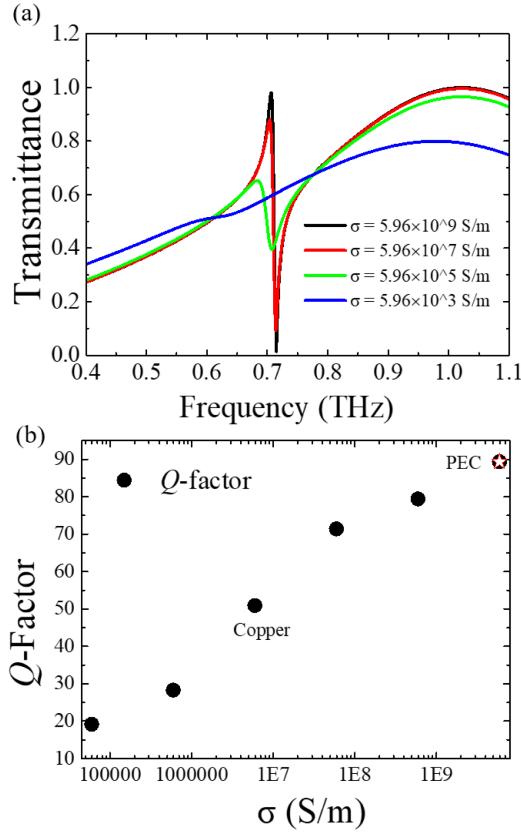


Fig. 3. (a) Transmittance spectra of HSAs with different conductivity ( $\sigma$ ). (b) The  $Q$ -factor versus different conductivities ( $\sigma$ ).

of the  $Q$ -factor among the quasi-BIC provides a simple route to engineer the periodic structures with the desired properties. But for the copper HSAs, due to the loss of the materials, the corresponding  $Q$ -factor cannot fit linear when the asymmetric parameter is relatively small. For example, when  $1/\delta^2$  is larger than 200, the red dot deviates from the black line. Hence, by controlling the asymmetric parameter, the quasi-BICs with a high  $Q$ -factor can be achieved.

$$\sigma_{\gamma} = \frac{\omega N e^2 / m}{(\omega_0^2 + \omega^2)^2 + \gamma^2 \omega^2} \quad (2)$$

As discussed in the previous session, the quasi-BIC is affected by the Ohmic loss of metal. Thus, the selection of materials is important for metal resonators. Here, the effects of different conductivities ( $\sigma$ ) on the resonant dips are simulated, where the length of  $L_2$  and sample thickness are kept as  $180 \mu\text{m}$  and  $50 \mu\text{m}$ , respectively. According to (2), where  $\gamma$  represents the Ohmic loss and  $\sigma$  denotes conductivity, it can be seen that conductivity is inversely proportional to the Ohmic loss [49],

As shown in Fig. 3(a), the dip of quasi-BICs becomes wide as the conductivity decreases from  $5.96 \times 10^9 \text{ S/m}$  to  $5.96 \times 10^3 \text{ S/m}$ , where  $\sigma = 5.96 \times 10^7 \text{ S/m}$  is the conductivity of copper. Specially, the quasi-BIC is disappeared when the conductivity is  $5.96 \times 10^3 \text{ S/m}$ . The  $Q$ -factor of quasi-BICs with various conductivity is summarized in Fig. 3(b). The  $Q$ -factor is about 20 when the conductivity is  $5.96 \times 10^5 \text{ S/m}$ . As the conductivity

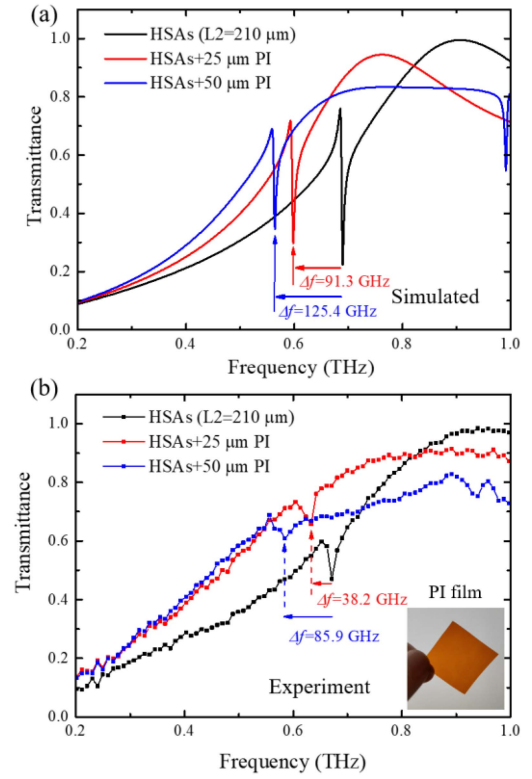


Fig. 4. (a) Simulated transmittance spectra of HSAs with  $25 \mu\text{m}$  and  $50 \mu\text{m}$  PI films. (b) Experimental transmittance spectra of HSAs with  $25 \mu\text{m}$  and  $50 \mu\text{m}$  PI films.

increases, the  $Q$ -factor increases. For example, the copper-HSA with a conductivity of  $5.96 \times 10^7 \text{ S/m}$  shows a  $Q$ -factor of 53. When the conductivity reaches 9 orders of magnitude, the  $Q$ -factor is close to 90, which equals that of PEC-HSAs. These results show that for a metal resonator with certain structural parameters, higher conductivity implies higher  $Q$ -factors.

### C. Sensing Performance of HSAs

As we have discussed in previous sections, the quasi-BICs with high  $Q$ -factors are important in sensing applications. Here, we investigated the sensing performance of HSAs-based sensors by covering a dielectric film. The refractive index of dielectric films is calculated by the experiment results, which depends on the frequencies. To simplify the simulation model, the dielectric film is selected as polyimide (PI) film with a refractive index of 1.61 at 0.6 THz. The materials absorption is not considered here because only resonant frequency shifts are recorded. Fig. 4(a) shows the transmittance spectra of HSAs with various film thicknesses, where  $L_2$  is  $210 \mu\text{m}$ . The pure HSAs shows a quasi-BIC dip at 0.686 THz, which shows a redshift when a PI film is attached. By varying the PI thickness from 0 to  $50 \mu\text{m}$ , the quasi-BIC shifts to lower frequencies, where the redshift ( $\Delta f$ ) for  $25 \mu\text{m}$  and  $50 \mu\text{m}$  PI are about 91.3 GHz and 125.4 GHz, respectively. The simulated results exhibit that the designed HSAs is sensitive to the analyte changes, which is promising for sensing applications. The corresponding experimental results are shown in Fig. 4(b). The redshift trend is consistent with

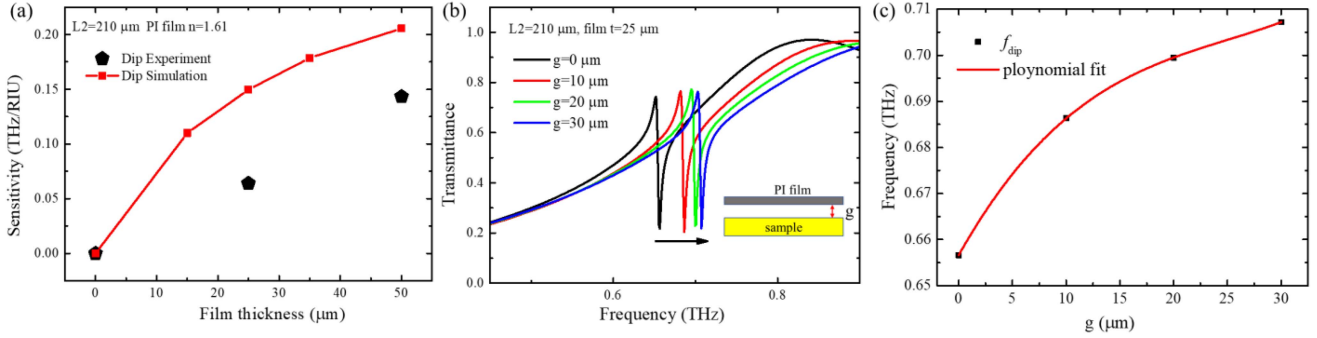


Fig. 5. (a) The sensitivity with different PI thicknesses for simulated and experiment. (b) Transmittance spectra of sensing model with different gaps between PI film and HSAs. (c) The resonant dip shifts with  $g$  increasing.

that of simulation results. Because of the imperfections in the experiment, the shift is about 38.2 GHz and 85.9 GHz for 25  $\mu\text{m}$  and 50  $\mu\text{m}$  PI, respectively. Such difference mainly comes from the gap between HSAs and PI films in the experiment, which will be detailedly discussed in the next section.

The sensitivity of HSAs with different film thicknesses is summarized in Fig. 5(a), where the sensitivity is defined as  $S = \Delta f / \Delta n$  in which  $\Delta n$  is the refractive index difference between the PI films and air space. Obviously, with the increasing PI thickness, the sensitivity is increased. The sensitivity is about 205.6 GHz/refractive index unit (RIU) when the PI is 50  $\mu\text{m}$ . The sensitivity for experiment results is also exhibited (black-dot). Due to the imperfection in the experiment, the difference between simulated and experiment exists. The experimental sensitivity is around 140.8 GHz/RIU for 50  $\mu\text{m}$ -PI. In the experiment, the PI film is attached to the surface of the sample, which leads to an air gap ( $g$ ) between the sample and the PI. To better understand the difference between experiment and simulated, we simulated the effect of the air gap between the PI and HSAs on the frequency shifts. The simulated results are present in Fig. 5(b), where the inset figure exhibits the definition of the air gap between PI and HSAs. The resonant dip shifts to high frequencies as  $g$  increases. The shift is about 30.3 GHz when  $g$  is 10  $\mu\text{m}$ . Fig. 5(c) shows the resonant dip shifts with  $g$  increasing, where the polynomial function is used for fitting. The resonant dip shift does not linearly increase as  $g$  increases, which becomes smooth when the gap is large because of the limited decay lengths of SPP fields. In contrast to that of the perfect simulated, these results demonstrated that the air gap leads to additional frequency shifts in the experiment.

#### D. Sensing Performance in Terms of the Film Thicknesses

To deeply explore the sensing potentials of HSAs, we investigated its sensing performance by using the perfect simulation results. In other words, the imperfections in the experiment is not considered. The figure of merit (FOM), which is defined as  $FOM = S/FWHM$ , was proposed as a more reasonable parameter to evaluate the performance of sensors [31], [50]. Fig. 6(a), (b) show the sensitivity and FOM for HSAs when  $L2$  length is 190  $\mu\text{m}$  and 210  $\mu\text{m}$ . The spectral peak originating from SPPs is selected as an example to compare. As shown in Fig. 6(a),

the sensitivities of the spectral peak and quasi-BICs dip are respectively about 147 GHz/RIU and 80 GHz/RIU when the thickness of PI films is 10  $\mu\text{m}$ . These sensitivities are higher than previous works of planar metamaterials with substrates [51]–[52]. However, due to the narrower bandwidth, the FOM for the quasi-BICs is found to be 7.54, which is higher than that of conventional resonances of 0.54. The higher FOM value benefits from the great suppression of the radiation scattering losses from the metallic structure because of the minimum scattering size [50]. Although the previous study concluded that the sensitivity of the conventional resonance peak is slightly higher, it is found that the resonance bandwidth is too wide to identify the position of its resonance peak as the thickness of the structural parameters increases. Therefore, a comprehensive study shows that the FOM is more favorable for evaluating its sensing performance. With the film thickness increasing, both sensitivity and FOM are improving. The slope of this trend is tightly associated with the decay length of the surface fields. We further investigated the sensing performance of HSAs when  $L2$  length is 210  $\mu\text{m}$ , the corresponding results are depicted in Fig. 6(b). The sensitivity and the FOM of the two resonances versus the variation of the dielectric film thickness are displayed. The sensitivity of the spectral peak is 82.1 GHz/RIU while that of the quasi-BICs is 118.8 GHz/RIU when the thickness of dielectric films is 10  $\mu\text{m}$ . In this case, the FOM corresponding for quasi-BICs is 10.2 while that of conventional resonance is 0.43. Compared to the 190- $\mu\text{m}$ - $L2$  quasi-BICs, the 210- $\mu\text{m}$ - $L2$  quasi-BICs obtain a higher FOM due to their narrower resonant bandwidth. Therefore, the FOM can be improved by increasing the sensitivity or decreasing the FWHM. Importantly, the quasi-BIC is also sensitive to the thin film with nano-scale thickness. Previous work has demonstrated that the quasi-BIC can be used to detect an analyte with a thickness of 7 nm [27]. Here, a typical 2D material of graphene consisting of a single atomic layer of hexagonal carbon lattice is tested [53]. As shown in Fig. 6(c), the quasi-BIC is obviously attenuated when an ultra-thin graphene film with a thickness of about 0.34 nm is attached.

#### E. Sensing Performance in Terms of Film Refractive Index

The refractive index of the analyte also has a giant effect on the sensing performances. Here, the thickness of the analyte is kept

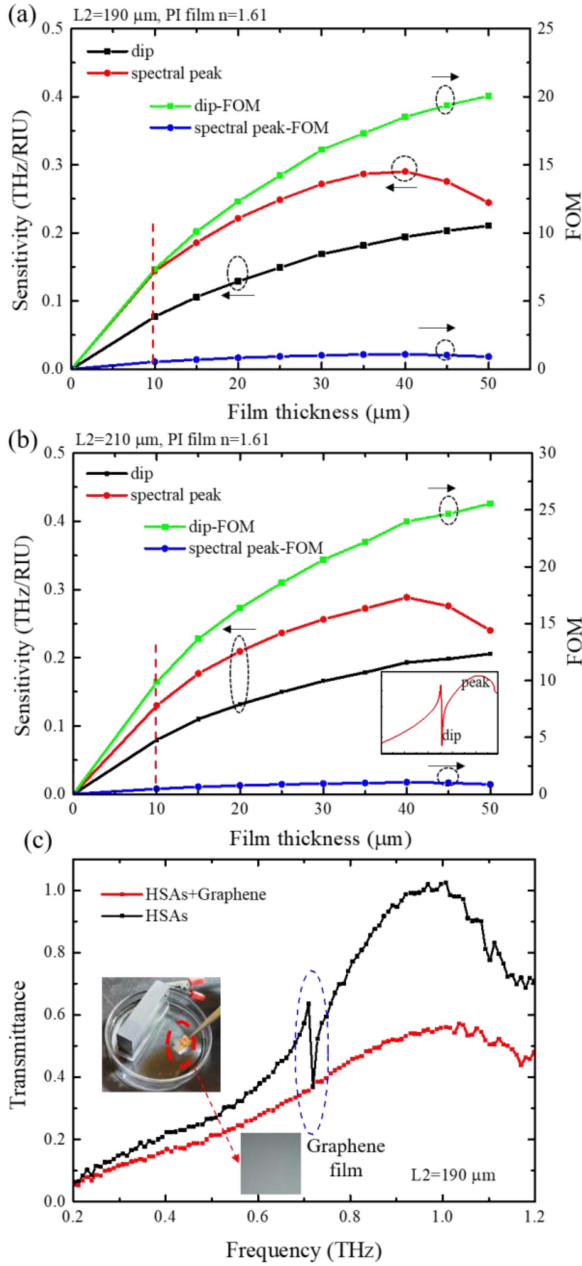


Fig. 6. (a) The sensitivity and FOM of HSAs ( $L_2 = 190 \mu\text{m}$ ) for the spectral peak and quasi-BICs dip. (b) The sensitivity and FOM of HSAs ( $L_2 = 210 \mu\text{m}$ ) for the spectral peak and quasi-BICs. (c) The spectral response when a graphene is attached.

at  $25 \mu\text{m}$ . Similarly, the frequency of two resonances decreases linearly with the increasing refractive index. According to  $S = \Delta f / \Delta n$  and  $FOM = S / FWHM$ , the slope of the results represents the value of sensitivity and FOM. As shown in Fig. 7(a), for the HSAs with  $L_2 = 190 \mu\text{m}$ , the sensitivity of the spectral peak is calculated to be  $256 \text{ GHz/RIU}$ . The frequency shift of the spectral peak for a film refractive index of 1.61 is  $152.7 \text{ GHz}$ , which is higher than the recorded sensitivity of some metamaterial sensors [31]. But the sensitivity for the quasi-BICs is about  $151 \text{ GHz/RIU}$ , which is lower than that of spectral peaks. The narrower resonant FWHM is very favorable for ultra-high

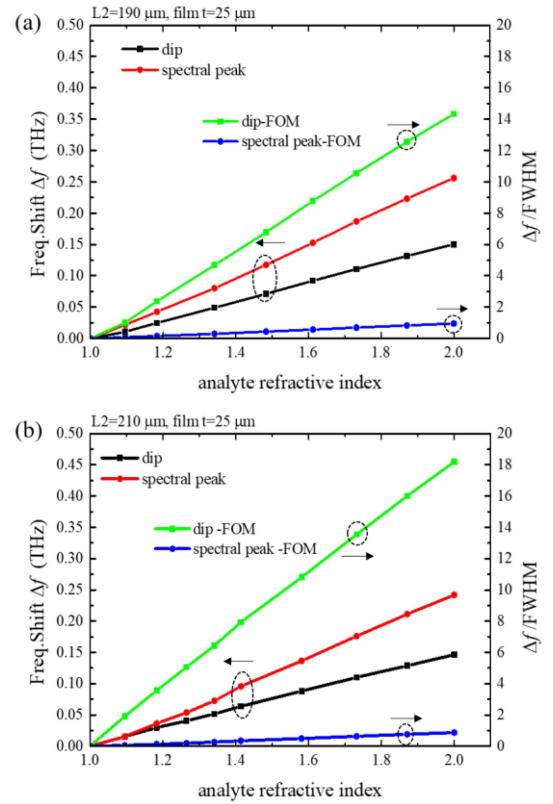


Fig. 7. (a) The frequency shift  $\Delta f$  and  $\Delta f / FWHM$  of HSAs ( $L_2 = 190 \mu\text{m}$ ) for the spectral peak and quasi-BICs with change in refractive indices. (b) The frequency shift  $\Delta f$  and  $\Delta f / FWHM$  of HSAs ( $L_2 = 210 \mu\text{m}$ ) for the spectral peak and quasi-BICs with change in refractive indices.

FOM. The quasi-BIC with an FWHM of  $10.485 \text{ GHz}$  achieved a FOM of  $14.38$ , which is about 15 times the conventional peak of  $0.95$ . The calculated frequency shift is shown in Fig. 7(b) when  $L_2 = 210 \mu\text{m}$ . As the refractive index of the analyte increases, the amount of change in the frequencies of the spectral peak and the quasi-BICs resonant dip increases. The sensitivity of the spectral peak is calculated to be  $242 \text{ GHz/RIU}$  while that of the quasi-BICs is  $146 \text{ GHz/RIU}$ . However, the dip of quasi-BICs shows a larger FOM than that of the spectral peak, which equals  $18.77$ . Compared with the results in Fig. 7(a), the  $210 \mu\text{m}$ - $L_2$  HSAs achieve a higher FOM than the  $190 \mu\text{m}$ - $L_2$  HSAs due to the narrower resonant bandwidth.

#### F. Sensing Performance in Terms of the Length of $L_2$

We summarized the sensing performance of HSAs with different  $L_2$ . As shown in Fig. 8(a), for a certain refractive index of 1.61, the sensitivity and FOM for both  $L_2 = 190$  and  $210 \mu\text{m}$ -HSAs increase as the film thickness increases. For HSAs with different  $L_2$ , the sensitivity is almost the same. For example, when the thickness is  $30 \mu\text{m}$ , the sensitivity of  $L_2 = 190 \mu\text{m}$  and  $L_2 = 210 \mu\text{m}$ -HSAs is about  $169$  and  $165 \text{ GHz/RIU}$ , respectively. But the FOM values are significant different. When the film thickness is  $20 \mu\text{m}$ , the FOM for  $L_2 = 210 \mu\text{m}$ -HSAs is  $16.4$ , while the FOM for  $L_2 = 90 \mu\text{m}$ -HSAs is  $12.3$ . With the thickness further increasing, the growth trend becomes flattened. It indicates that the film thickness is larger than the field decay

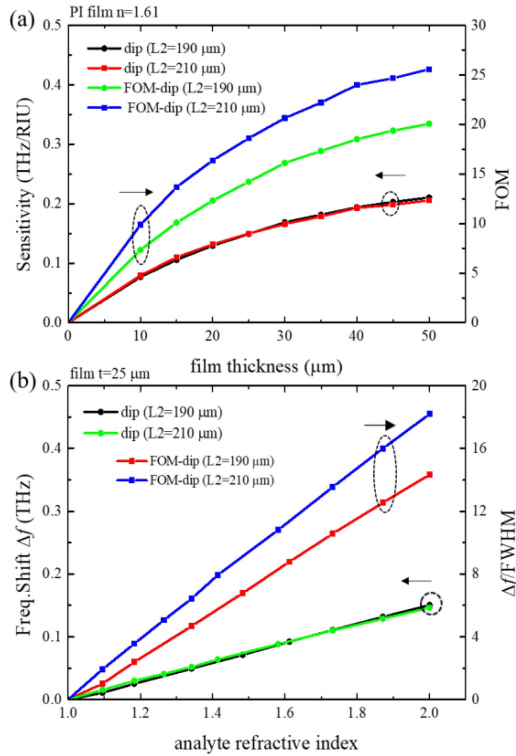


Fig. 8. (a) The sensitivity and FOM of quasi-BICs for the HSAs with different  $L2$ , where the refractive index of the film is 1.61. (b) Frequency shift ( $\Delta f$ ) and  $\Delta f/FWHM$  with change in refractive indices, where the thickness of films is 25  $\mu\text{m}$ .

TABLE I  
THE PERFORMANCE FOR DIFFERENT SENSOR DESIGNS

Reference	Operating band (THz)	Material ( $n$ )	$Q$ -factor	Sensitivity (GHz/RIU)	FOM(/RIU)
[55]	0.15-0.85	1.73	--	139.2	2.51
[32]	0.3-0.6	1.41	--	128	1.82
[56]	0.6-0.9	2	--	36.96	1.60
[27]	0.4-1.8	1.48	--	10.8	38.1
[57]	1.71-1.81	1.09	462.62	6 $\mu\text{m}$ /RIU	16.22
[54]	0.4-0.9	1.6	11	128.48	1.98
<b>This work</b>	<b>0.2-1.2</b>	<b>1.61</b>	<b>180</b>	<b>151</b>	<b>18.7</b>

length. Next, the sensing performance of HSAs with different  $L2$  at a certain thickness is investigated. The sensitivity and coefficient of quasi-BICs are shown in Fig. 8(b). Similar to the results in Fig. 8(a), the difference in sensitivity between 190  $\mu\text{m}$ - and 210  $\mu\text{m}$ - $L2$  is small. The frequency shift is about 151 GHz when the refractive index is 2.0. Interestingly, the slope for the frequency shift is kept the same, which can also be observed for the  $\Delta f/FWHM$ . The  $\Delta f/FWHM$  is increasing monotonically as the film refractive index increases, where  $L2 = 210 \mu\text{m}$  shows a higher value than that of  $L2 = 190 \mu\text{m}$  because of the narrower resonant bandwidth. Therefore, a proper method to improve sensor performance is to reduce the bandwidth of resonances.

Finally, we have compared our structure with other designs in the literature. The performance of the different sensors is summarized in Table I. In [32], the proposed MHAs realize a sensitivity of 128 GHz/RIU and FOM of 1.82 based on the lowest SPPs mode, where the analyte thickness is 50  $\mu\text{m}$ . In [54], a

metasurface is composed of two perpendicularly intersecting metallic bars with a cylindrical metallic element in the middle. Numerical results show that such sensor obtains a sensitivity, FOM, and  $Q$ -factor of 6  $\mu\text{m}$ /RIU, 16.22 1/RIU, and 462.62 respectively. In this work, we have used quasi-BICs for the material senses, which achieve a sensitivity of 151 and FOM of 18.7 for 25  $\mu\text{m}$ -analyte. The use of the quasi-BICs instead of regular resonances realizes higher sensing performances [54], [55], [56], [57], [58], [59].

## CONCLUSION

In this work, an all-metal sensing based on HSAs is numerically and experimentally investigated at terahertz frequencies. The symmetry-protected BICs are activated by adjusting one arm's length of the H-shaped, enabling high- $Q$  quasi-BICs. Simulated results show that the proposed HSAs achieve a simulated high  $Q$ -factor of 180. Due to the limited solution of the measurement system, the measured  $Q$ -factor is 75. The  $Q$ -factor of quasi-BICs is also tunable in terms of structural parameters and metal conductivity. For a metal resonator with certain structural parameters, higher conductivity implies higher  $Q$ -factors. With optimal structural parameters of copper HSAs, the proximity sensing performances are studied in detail, including the film thickness and the refractive index. High sensitivity and FOM of 151 GHz/RIU and 18.7 are respectively obtained, which are high compared with the previous metamaterials with planar substrates. Furthermore, the HSAs are even sensitive to the ultrathin graphene film. Experimental results proved that the quasi-BICs can be attenuated by a 0.34 nm-thick graphene. These findings indicate that the sensor has great potential for practical applications in chemical and biomolecular areas.

## ACKNOWLEDGMENT

L. Wang created the design, performed the simulation, and wrote the manuscript. F. Liu guided the project and supplied the experimental system. D. Liu guided the project, performed theoretical analysis, measurement, data analysis, and wrote the manuscript. All authors have contributed to the organization and writing of this manuscript.

*Disclosures:* The authors declare no conflicts of interest.

## REFERENCES

- [1] C. M. Linton and P. Mciver, "Embedded trapped modes in water waves and acoustics," *Wave Motion*, vol. 45, no. 1, pp. 16–29, 2007.
- [2] T. Lapetit and B. Kanté, "Controlling multipolar radiation with symmetries for electromagnetic bound states in the continuum," *Phys. Rev. B*, vol. 90, no. 24, 2014, Art. no. 241103.
- [3] D. C. Marinica, A. G. Borisov, and S. V. Shabanov, "Bound states in the continuum in photonics," *Phys. Rev. Lett.*, vol. 100, no. 18, 2008, Art. no. 183902.
- [4] E. N. Bulgakov and A. F. Sadreev, "Bound states in the continuum in photonic waveguides inspired by defects," *Phys. Rev. B*, vol. 78, no. 7, 2008, Art. no. 075105.
- [5] F. Dreisow et al., "Adiabatic transfer of light via a continuum in optical waveguides," *Opt. Lett.*, vol. 34, no. 16, pp. 2405–2407, 2009.
- [6] Y. Plotnik et al., "Experimental observation of optical bound states in the continuum," *Phys. Rev. Lett.*, vol. 107, no. 18, 2011, Art. no. 183901.
- [7] S. Weimann et al., "Compact surface Fano states embedded in the continuum of waveguide arrays," *Phys. Rev. Lett.*, vol. 111, no. 24, 2013, Art. no. 240403.

- [8] C. W. Hsu et al., "Observation of trapped light within the radiation continuum," *Nature*, vol. 499, no. 7457, pp. 188–191, 2013.
- [9] F. Monticone and A. Alù, "Embedded photonic eigenvalues in 3D nanostructures," *Phys. Rev. Lett.*, vol. 112, no. 21, pp. 112–115, 2014.
- [10] M. I. Molina, A. E. Miroshnichenko, and Y. S. Kivshar, "Surface bound states in the continuum," *Phys. Rev. Lett.*, vol. 108, no. 7, 2012, Art. no. 070401.
- [11] M. Rybin and Y. Kivshar, "Supercavity lasing," *Nature*, vol. 541, no. 7636, pp. 164–165, 2017.
- [12] S. Campione et al., "Broken symmetry dielectric resonators for high quality factor Fano metasurfaces," *ACS Photon.*, vol. 3, no. 12, pp. 2362–2367, 2016.
- [13] A. Taghizadeh and I. S. Chung, "Quasi bound states in the continuum with few unit cells of photonic crystal slab," *Appl. Phys. Lett.*, vol. 111, no. 3, 2017, Art. no. 031114.
- [14] W. Liu, Y. Sun, Z. Lai, and H. Chen, "Sharp optical magnetic resonances in dielectric waveguide grating structures," *J. Opt. Soc. Amer. B*, vol. 34, no. 9, pp. 1899–1940, 2017.
- [15] E. N. Bulgakov, D. N. Maksimov, P. N. Semina, and S. A. Skorobogatov, "Propagating bound states in the continuum in dielectric gratings," *J. Opt. Soc. Amer. B*, vol. 35, no. 6, pp. 1218–1222, 2018.
- [16] K. Koshelev, S. Lepeshov, M. Liu, A. Bogdanov, and Y. Kivshar, "Asymmetric metasurfaces with high-Q resonances governed by bound states in the continuum," *Phys. Rev. Lett.*, vol. 121, no. 19, 2018, Art. no. 193903.
- [17] F. Wu et al., "Giant enhancement of the Goos-Hänchen shift assisted by quasibound states in the continuum," *Phys. Rev. Appl.*, vol. 12, no. 1, 2019, Art. no. 014028.
- [18] S. Romano et al., "Label-free sensing of ultralow-weight molecules with all-dielectric metasurfaces supporting bound states in the continuum," *Photon. Res.*, vol. 6, no. 7, pp. 726–733, 2018.
- [19] X. Wang, S. Li, and C. Zhou, "Polarization-independent toroidal dipole resonances driven by symmetry-protected BIC in ultraviolet region," *Opt. Exp.*, vol. 28, no. 8, pp. 11983–11989, 2020.
- [20] L. S. Li and C. H. Yin, "Bound states in the continuum in double layer structures," *Sci. Rep.*, vol. 6, no. 1, pp. 1–8, 2016.
- [21] Y. Han, W. Gong, and G. Wei, "Bound states in the continuum in electronic transport through parallel-coupled quantum-dot structures," *Phys. Status Solidi B*, vol. 246, no. 7, pp. 1634–1641, 2010.
- [22] J. Lee et al., "Observation and differentiation of unique high-Q optical resonances near zero wave vector in macroscopic photonic crystal slabs," *Phys. Rev. Lett.*, vol. 109, no. 6, 2012, Art. no. 067401.
- [23] G. Corrielli, V. G. Della, A. Crespi, R. Osellame, and S. Longhi, "Observation of surface states with algebraic localization," *Phys. Rev. Lett.*, vol. 111, no. 22, 2013, Art. no. 220403.
- [24] Y. S. Lee, *Principles of Terahertz Science and Technology*, vol. 170. Berlin, Germany: Springer Science & Business Media, 2009.
- [25] K. E. Peiponen, A. Zeitler, and M. Kuwata-Gonokami, *Terahertz Spectroscopy and Imaging*. Berlin, Germany: Springer, 2012.
- [26] S. Han et al., "All-dielectric active terahertz photonics driven by bound states in the continuum," *Adv. Mater.*, vol. 31, no. 37, 2019, Art. no. 1901921.
- [27] Y. K. Srivastava, R. T. Ako, M. Gupta, M. Bhaskaran, S. Sriram, and R. Singh, "Terahertz sensing of 7nm dielectric film with bound states in the continuum metasurfaces," *Appl. Phys. Lett.*, vol. 115, no. 15, 2019, Art. no. 151105.
- [28] X. Chen, W. Fan, and H. Yan, "Toroidal dipole bound states in the continuum metasurfaces for terahertz nanofilm sensing," *Opt. Exp.*, vol. 28, no. 11, pp. 17102–17112, 2020.
- [29] R. Singh, W. Cao, I. Al-Naib, L. Cong, W. Withayachumnankul, and W. Zhang, "Ultrasensitive terahertz sensing with high-Q Fano resonances in metasurfaces," *Appl. Phys. Lett.*, vol. 105, no. 17, 2014, Art. no. 171101.
- [30] W. Lim, M. Manjappa, P. Pitchappa, and R. Singh, "Shaping high-Q planar Fano resonant metamaterials toward futuristic technologies," *Adv. Opt. Mater.*, vol. 6, no. 19, 2018, Art. no. 1800502.
- [31] M. Beruete and I. Jáuregui-López, "Terahertz sensing based on metasurfaces," *Adv. Opt. Mater.*, vol. 8, no. 3, 2020, Art. no. 1900721.
- [32] R. Yahiaoui, A. C. Strikwerda, and P. U. Jepsen, "Terahertz plasmonic structure with enhanced sensing capabilities," *IEEE Sensors J.*, vol. 16, no. 8, pp. 2484–2488, Apr. 2016.
- [33] S. Yoshida, K. Suiizu, E. Kato, Y. Nakagomi, and Y. Ogawa, and K. Kawase, "A high-sensitivity terahertz sensing method using a metallic mesh with unique transmission properties," *J. Mol. Spectrosc.*, vol. 256, no. 1, pp. 146–151, 2009.
- [34] T. Hasebe, Y. Yamada, and H. Tabata, "Label-free THz sensing of living body-related molecular binding using a metallic mesh," *Biochem. Biophysical Res. Commun.*, vol. 414, no. 1, pp. 192–198, 2011.
- [35] D. Liu and T. Hattori, "Sharp resonances in terahertz free-standing three-dimensional metallic woven meshes," *Opt. Exp.*, vol. 28, no. 20, pp. 30174–30186, 2020.
- [36] F. Miyamaru et al., "Terahertz surface-wave resonant sensor with a metal hole array," *Opt. Lett.*, vol. 31, no. 8, pp. 1118–1120, 2006.
- [37] T. Hasebe, S. Kawabe, H. Matsui, and H. Tabata, "Metallic mesh-based terahertz biosensing of single-and double-stranded DNA," *J. Appl. Phys.*, vol. 112, no. 9, 2012, Art. no. 094702.
- [38] H. Yoshida et al., "Terahertz sensing method for protein detection using a thin metallic mesh," *Appl. Phys. Lett.*, vol. 91, no. 25, 2007, Art. no. 253901.
- [39] Z. Liu, H. Li, H. Xu., G. Cao, X. Xu, and H. Yang, "Adjustable plasmon resonances through an H-shaped metallic grating," *Opt. Commun.*, vol. 285, no. 18, pp. 3781–3786, 2012.
- [40] X. Yu, Y. Yasunaga, K. Goto, D. Liu, and S. Ono, "Profile control of femtosecond laser-fabricated moth-eye structures on Si substrate," *Opt. Laser Eng.*, vol. 142, 2021, Art. no. 106584.
- [41] Y. Zhang et al., "High-quality-factor multiple Fano resonances for refractive index sensing," *Opt. Lett.*, vol. 43, no. 8, pp. 1842–1845, 2018.
- [42] D. Liu, F. Wu, R. Yang, L. Chen, X. He, and F. Liu, "Quasi-bound states in the continuum in metal complementary periodic cross-shaped resonators at terahertz frequencies," *Opt. Lett.*, vol. 46, no. 17, pp. 4370–4373, 2021.
- [43] L. Chen, D. Liao, X. Guo, J. Zhao, Y. Zhu, and S. Zhuang, "Terahertz time-domain spectroscopy and micro-cavity components for probing samples: A review," *Front. Inf. Technol. Electron. Eng.*, vol. 20, no. 5, pp. 591–607, 2019.
- [44] X. Zhao et al., "Terahertz investigation of bound states in the continuum of metallic metasurfaces," *Optica*, vol. 7, no. 11, pp. 1548–1554, 2020.
- [45] W. Cao, R. Singh, I. A. I. Al-Naib, M. He, A. J. Taylor, and W. Zhang, "Low-loss ultra-high-Q dark mode plasmonic Fano metamaterials," *Opt. Lett.*, vol. 37, no. 16, pp. 3366–3368, 2012.
- [46] B. Luk'yanchuk et al., "The Fano resonance in plasmonic nanostructures and metamaterials," *Nature Mater.*, vol. 9, no. 9, pp. 707–715, 2010.
- [47] C. Cui et al., "Multiple Fano resonances in symmetry-breaking silicon metasurface for manipulating light emission," *ACS Photon.*, vol. 5, no. 10, pp. 4074–4080, 2018.
- [48] C. W. Hsu, B. Zhen, A. D. Stone, J. D. Joannopoulos, and M. Soljačić, "Bound states in the continuum," *Nature Rev. Mater.*, vol. 1, no. 9, pp. 1–13, 2016.
- [49] D. J. Griffiths, *Introduction to Electrodynamics*. Upper Saddle River, NJ, USA: Prentice Hall, 2005.
- [50] B. Liu et al., "A plasmonic sensor array with ultrahigh figures of merit and resonance linewidths down to 3 nm," *Adv. Mater.*, vol. 30, no. 12, 2018, Art. no. 1706031.
- [51] R. Singh, I. A. I. Al-Naib, M. Koch, and W. Zhang, "Sharp Fano resonances in THz metamaterials," *Opt. Exp.*, vol. 19, no. 7, pp. 6312–6319, 2011.
- [52] L. Cong, M. Manjappa, N. Xu, I. Al-Naib, W. Zhang, and R. Singh, "Fano resonances in terahertz metasurfaces: A figure of merit optimization," *Adv. Opt. Mater.*, vol. 3, no. 11, pp. 1537–1543, 2015.
- [53] W. Liu et al., "Graphene-enabled electrically controlled terahertz metasurfaces," *Photon. Res.*, vol. 6, no. 7, pp. 703–708, 2018.
- [54] L. Cong, S. Tan, R. Yahiaoui, F. Yan, W. Zhang, and R. Singh, "Experimental demonstration of ultrasensitive sensing with terahertz metamaterial absorbers: A comparison with the metasurfaces," *Appl. Phys. Lett.*, vol. 106, 2015, Art. no. 031107.
- [55] R. Yahiaoui, S. Tan, L. Cong, R. Singh, F. Yan, and W. Zhang, "Multispectral terahertz sensing with highly flexible ultrathin metamaterial absorber," *J. Appl. Phys.*, vol. 118, no. 8, 2015, Art. no. 083103.
- [56] I. Jáuregui-López, P. Rodríguez-Ulibarri, S. A. Kuznetsov, N. A. Nikolaev, and M. Beruete, "THz sensing with anomalous extraordinary optical transmission hole arrays," *Sensors*, vol. 18, no. 11, 2018, Art. no. 3848.
- [57] M. Askari, H. Pakarzadeh, and F. Shokrgozar, "High Q-factor terahertz metamaterial for superior refractive index sensing," *J. Opt. Soc. Amer. B*, vol. 38, no. 12, pp. 3929–3936, 2021.
- [58] M. A. Habib, M. S. Anower, L. F. Abdulrazak, and M. S. Reza, "Hollow core photonic crystal fiber for chemical identification in terahertz regime," *Opt. Fiber Technol.*, vol. 52, 2019, Art. no. 101933.
- [59] H. Pakarzadeh, V. Sharif, D. Vigneswaran, and N. Ayyanar, "Graphene-assisted tunable D-shaped photonic crystal fiber sensor in the visible and IR regions," *J. Opt. Soc. Amer. B*, vol. 39, no. 6, pp. 1490–1496, 2022.